

Characterization of gas shale pore systems by porosimetry, pycnometry, surface area, and field emission scanning electron microscopy/transmission electron microscopy image analyses: Examples from the Barnett, Woodford, Haynesville, Marcellus, and Doig units

Gareth R. Chalmers, R. Marc Bustin, and Ian M. Power

ABSTRACT

The nanometer-scaled pore systems of gas shale reservoirs were investigated from the Barnett, Marcellus, Woodford, and Haynesville gas shales in the United States and the Doig Formation of northeastern British Columbia, Canada. The purpose of this article is to provide awareness of the nature and variability in pore structures within gas shales and not to provide a representative evaluation on the previously mentioned North American reservoirs. To understand the pore system of these rocks, the total porosity, pore-size distribution, surface area, organic geochemistry, mineralogy, and image analyses by electron microscopy were performed. Total porosity from helium pycnometry ranges between 2.5 and 6.6%. Total organic carbon content ranges between 0.7 and 6.8 wt. %, and vitrinite reflectance measured between 1.45 and 2.37%.

AUTHORS

GARETH R. CHALMERS ~ *Earth and Ocean Sciences, University of British Columbia, 6339 Stores Road, Vancouver, British Columbia, Canada V6T 1Z4; gchalmers@eos.ubc.ca*

Gareth R. L. Chalmers is a postdoctoral research fellow at the Department of Earth and Ocean Sciences at the University of British Columbia, focusing on geologic controls of liquid and gas shale reservoirs. He is the global director of Chalmcoal Consulting and received his Ph.D. from the University of British Columbia.

R. MARC BUSTIN ~ *Earth and Ocean Sciences, University of British Columbia, 6339 Stores Road, Vancouver, British Columbia, Canada V6T 1Z4; bustin@interchange.ubc.ca*

R. Marc Bustin is a professor of petroleum and coal geology in the Department of Earth and Ocean Sciences at the University of British Columbia and president of RMB Earth Science Consultants. Bustin is an elected fellow of the Royal Society of Canada.

IAN M. POWER ~ *Earth and Ocean Sciences, University of British Columbia, 6339 Stores Road, Vancouver, British Columbia, Canada V6T 1Z4; ipower@eos.ubc.ca*

Ian Power is a postdoctoral fellow in the Department of Earth and Ocean Sciences at the University of British Columbia. His research integrates geomicrobiology and low-temperature geochemistry for the study of mineral carbonation processes and their applications for carbon sequestration.

ACKNOWLEDGEMENTS

We thank Natural Sciences and Engineering Research Council and Geosciences British Columbia for their financial support of the research. We also thank AAPG Editor Stephen Laubach and the reviewers R. Koepnick and K. Milliken for their comments and suggestions.

The AAPG Editor thanks the following reviewers for their work on this paper: Richard B. Koepnick and Kitty L. Milliken.

Copyright ©2012. The American Association of Petroleum Geologists. All rights reserved.

Manuscript received April 16, 2011; provisional acceptance August 11, 2011; revised manuscript received September 26, 2011; final acceptance October 17, 2011.

DOI:10.1306/10171111052

The gas shales in the United States are clay and quartz rich, with the Doig Formation samples being quartz and carbonate rich and clay poor. Higher porosity samples have higher values because of a greater abundance of mesopores compared with lower porosity samples. With decreasing total porosity, micropore volumes relatively increase whereas the sum of mesopores and macropore volumes decrease. Focused ion beam milling, field emission scanning electron microscopy, and transmission electron microscopy provide high-resolution (~ 5 nm) images of pore distribution and geometries. Image analysis provides a visual appreciation of pore systems in gas shale reservoirs but is not a statistically valid method to evaluate gas shale reservoirs. Macropores and mesopores are observed as either intergranular porosity or are confined to kerogen-rich aggregates and show no preferred orientation or align parallel with the laminae of the shale. Networks of mesopores are observed to connect with the larger macropores within the kerogen-rich aggregates.

INTRODUCTION

The ability to economically produce gas and light liquid hydrocarbons from rocks that have traditionally been considered both the source and seals to conventional reservoir rocks has forced a paradigm shift in our understanding of the pore structure of low-permeability rocks. Understanding the pore structure of these rocks has been hindered by our lack of tools to investigate their pore structure. The application of tools and techniques used to characterize traditional reservoir rocks provides consistent, albeit commonly erroneous, results for shale reservoirs. In addition, it is difficult to generalize about the pore structure of these so-called shales because rocks that are being referred to as gas shales or oil-producing shales (shale oil) include lithologies of various degrees of diagenesis and include rocks that are true shale, mudstones, limestones, dolomite, porcellenites, and sandstones to name a few. Shale is defined as laminated fine-grained argillaceous rock (Potter

et al., 2005; Boggs, 2012). Because geology is particularly a visual discipline, geologists have been strongly motivated to image the pore structure of shales although the scanning electron microscope cannot image a large proportion of the finest pore structure of shales (Marschall et al., 2005). In other disciplines, such as chemical engineering and surface chemistry, the study of microporous material is more advanced and some of these methods are portable to the study of shales, albeit the techniques are not in the tool box of most shale geologists or engineers. In this article, we bring together several state-of-the-art methods of characterizing microporous materials to provide an appreciation for the pore structure of some important gas shales. Here, we examine samples from producing strata of the Barnett, Marcellus, Woodford, Haynesville, and Doig units that represent a range of lithology and maturity. We do not propose to represent these formations by these samples in as much as these units are heterogeneous and the sample size is small, but instead we attempt to provide awareness of the nature and variability in pore structure.

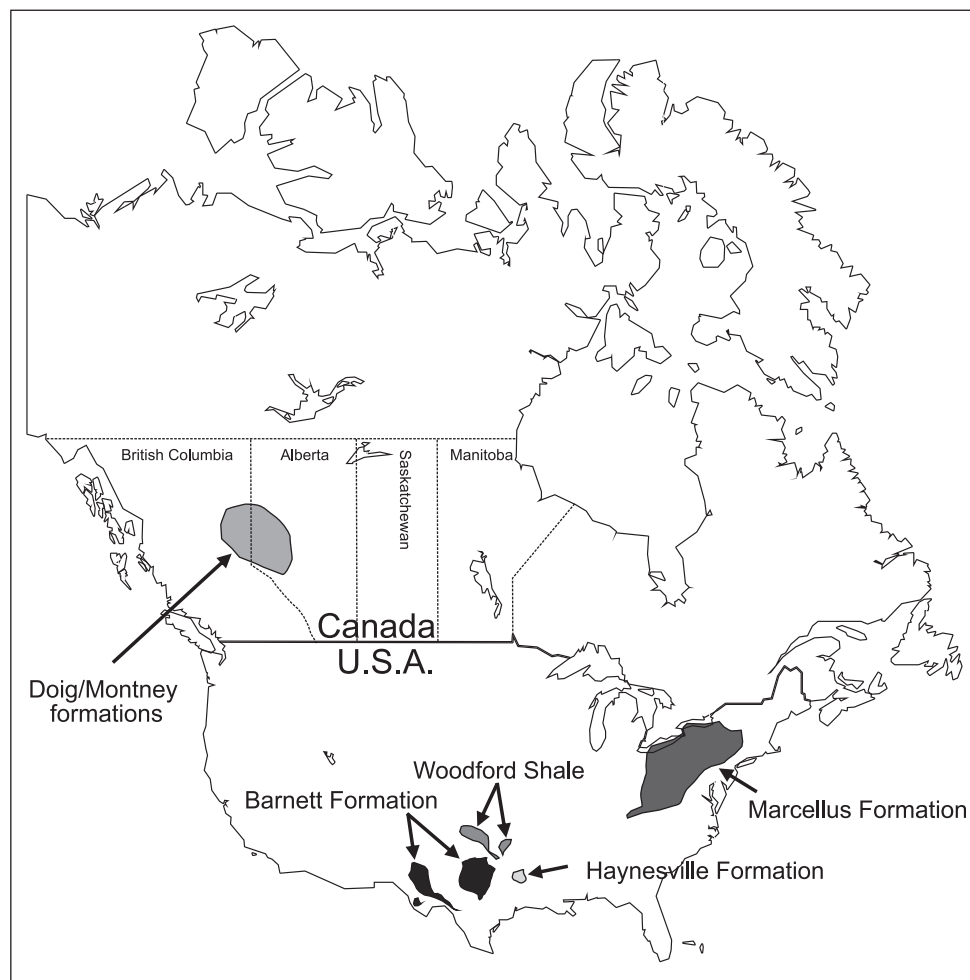
The nanometer-scaled pore systems of gas shales are an important control on hydrocarbon storage capacity and fluid transmissivity to fracture networks. The ability to produce, store, and transmit hydrocarbons are fundamental properties of economically producing self-sourced reservoirs like gas shales. Pores within gas shale reservoirs are an order of magnitude smaller (nanometer scale) than pores within conventional carbonate and sandstone reservoirs (micrometer scale; i.e., Nelson, 2009). Previous work on describing the pore-size distribution in gas shale has been ad hoc, with pores being loosely classified as nanopores in some studies (i.e., Javadpour, 2009; Loucks et al., 2009). A pore classification system already exists for materials that contain nanometer-scaled porosity that categorizes pore sizes based on physical adsorption properties and capillary condensation theory (Gregg and Sing, 1982; IUPAC, 1994; Zdravkov et al., 2007). Pores are subdivided into the three categories: macropores (>50 nm), mesopores (2–50 nm), and micropores (<2 nm) (IUPAC, 1994). The lower limit of micropores will depend on the kinetic diameter of

the probing gas molecule (i.e., 0.35 nm for carbon dioxide). These pore categories are important when considering unconventional gas reservoirs (organic-rich shales and coals) because a significant part of the gas can be found in the sorbed state within the mesopores and micropores (Gan et al., 1972; Marsh, 1987; Unsworth et al., 1989; Lamberson and Bustin, 1993; Clarkson and Bustin, 1996; Chalmers and Bustin, 2007, 2008; Ross and Bustin, 2007, 2008). An inverse relationship exists between pore size and surface area (Beliveau, 1993), and research has shown that micropores contribute more to the total surface area (sorption site for methane) than mesopores, whereas macropores contribute the least. For example, studies in organic-rich sludge (Lu et al., 1995), coals (Beliveau, 1993; Mastalerz et al., 2008), and shales (Chalmers and Bustin, 2007, 2008; Ross and Bustin, 2009) show surface area increases with a greater volume of micropores. Porosity develops within kerogen during thermal decomposition and generation of hydrocarbons (i.e., Jarvie et al., 2007). Microporosity increases within the kerogen with increasing maturity (Chalmers and Bustin, 2008; Ross and Bustin, 2009) and with the simultaneous development of microporous surface area and hydrocarbons, little to no migration of hydrocarbons is necessary (i.e., self-sourced reservoir). Further research is needed to identify whether gas shale micropores are water wet. Mesopores and micropores are economically important to gas shale production because of their large contribution to shale porosity (Keller et al., 2011) and storage sites (surface area) for sorbed methane. Methane transport mechanisms within the nanometer-scaled pore system include both diffusion (molecular flow) and advection (Darcy flow) (Schlomer and Krooss, 1997).

Transmitted and reflected light microscopy cannot image mesopores and micropores because of low power of magnification (1000 \times) compared with electron microscopy (500,000 \times). Rock chips in a scanning electron microscopy (SEM) cannot be used to observe mesopores and micropores because of the irregular surface topography. Because these techniques cannot adequately characterize the nanometer-scale pore systems in gas shale reservoirs, proxies like gas adsorption analyses, nuclear magnetic resonance (i.e., Sigal and

Oduşina, 2011) and mercury porosimetry are used to define the pore-size distribution (PSD). The PSD of mesopores and macropores using gas adsorption analyses are based on the Brunauer, Emmett, and Teller (BJH) (Barrett et al., 1951) model using nitrogen as a probe gas with carbon dioxide used for determining the PSD of micropores based on the Dollimore and Heal (Dollimore and Heal, 1964) model. Both models assume cylindrical-shaped pores. Physisorption (van der Waal forces) and capillary action occur in microporosity and mesoporosity, with the latter being more common with the mesopore size fraction (Gregg and Sing, 1982). Atomic force microscopy has been used to image mesopores in fine-grained rocks (Javadpour, 2009); however, resolution of these pore structures is poor whereas micropores have not been imaged. Innovations in electron microscopy have led to the development of the focused ion beam (FIB) milling technique, higher magnification (800,000 \times) field emission SEM (FE-SEM), and transmission electron microscopy (TEM), which has provided a tool for visualization of pore systems that were too fine to observe by other methods of microscopy. The FIB milling techniques remove topographic features and produce flat surfaces (Keller et al., 2011) for high-magnification FE-SEM and TEM observations. This combination allows the observation of fine macropores and mesopores within shale reservoirs. Keller et al. (2011) show both two-dimensional and three-dimensional (3-D) pore structures using a similar milling technique in the mesopore and macropore size ranges. Transmission electron microscopy is an imaging technique that is dependent on the interaction of the electron as it moves through the material. The changes in contrast within a TEM image are based on the electron density differences because of either the thickness or the composition of the material and has been used in many geologic materials (i.e., Dong and Peacor, 1996; Fisher et al., 2003; Nemeth et al., 2007). The TEM provides images of pore structures within thinly milled thin sections (<100 nm), and because of this thinness, a single image can capture macropores and mesopores throughout the thickness of the thin section and provide a pseudo-3-D structure of the pore system.

Figure 1. Geographical location of the subcrop boundaries of the Barnett, Doig, Haynesville, Marcellus, and Woodford shales.



The purpose of this article is to provide both quantitative and visual qualitative analyses of the gas shale reservoir pore system. Quantitative analyses by mercury porosimetry and low-pressure gas adsorption were used to determine the PSD of five North American gas shales and identify relationships between the PSD and the fabric, texture, composition, and geochemistry of the shale. The PSD is between 3 nm and 123 μm based on mercury porosimetry and between 0.35 and 300 nm for gas adsorption analysis. A qualitative approach toward TEM and FE-SEM image analyses is required as a quantitative reservoir characterization by FE-SEM image analysis would result in significant errors because of upscaling to a laterally and stratigraphically highly variable reservoir. This article will also discuss the limitations of the use of FE-SEM and TEM image analyses in the characterization of the shale reservoir pore system.

METHODOLOGY AND ANALYTICAL LIMITATIONS

Six samples obtained from drill cuttings, one each from the Barnett, Marcellus, Woodford, and Haynesville units and two from the Doig Formation were analyzed to characterize pore structure, geometry, and distribution. Only drill cutting samples were available for this study, and no comparison can be made with petrographic thin sections. The location of each sample is shown in Figure 1. The two Doig Formation samples differ in lithology with a fine-grained clay- and carbonate-rich sample referred to as the Doig phosphate and a coarser grained quartz-rich sample referred to as the Doig siltstone. The total porosity, PSD, mineralogy, organic geochemistry, organic petrology, FE-SEM and TEM image, and energy-dispersive spectrometry (EDS) analyses were performed on each sample. The mineralogical

composition adjacent to pore structures is identified using elemental analysis (EDS) and bulk mineralogy from x-ray diffraction. We separated the mesopore-size fraction into coarse (25–50 nm), medium (25–10 nm), and fine mesopores (2–10 nm) to aid the description of each sample. To image mesopores, samples were not coated, and a low voltage (i.e., 1 kV) was used to prevent sample charging. Under those conditions, backscatter electron microscopy was not suitable.

Pore-Size Distribution

Pore-size distribution of gas shales is measured using both mercury porosimetry and low-pressure gas adsorption analyses. Samples are crushed (2–4 mm) and oven dried (110°C), evacuated to 1×10^{-4} psia, and intruded with mercury from 1.5 to 60,000 psia using a Micromeritics™ Autopore IV 9500 series apparatus. The measured pressure range equates to the pore diameter range of 3 to 1.2×10^5 nm. The minimal pore diameter limit of 3 nm is within the mesopore range, and mercury porosimetry cannot detect micropores within the pore system.

Low pressure (<18.4 psia) gas adsorption analyses using both nitrogen and carbon dioxide probe gases have been used to measure the PSD between the pore diameters of 0.35 and 300 nm (Quantachrome, 2008). Although carbon dioxide is being used as the probe gas, the PSD limit of 0.35 nm is still relevant to methane (kinetic diameter of 0.38 nm). Between 1 and 2 g of ground sample (<250 μm) is degassed at 70°C for 12 hr before analysis. Samples need to be crushed to less than 250 μm to reach the vacuum threshold to begin the gas adsorption analysis. The PSD will differ slightly between the two techniques (porosimetry and gas adsorption analyses) because of sample preparation. Carbon dioxide (CO₂) adsorption is coupled with the N₂ adsorption analysis to examine the micropore size fraction as the analytical temperature of N₂ adsorption analyses is too low (–196°C) for nitrogen molecules to access the fine micropores (Unsworth et al., 1989). The analytical temperature used for CO₂ adsorption

analysis (0°C) provides the necessary kinetic energy for the CO₂ molecule to access the micropores. The surface area of micropores was determined by CO₂ adsorption using the Dubinin-Radushkevich (D-R) equation and using the cross sectional area of the CO₂ molecule of 0.253 nm² (Clarkson and Bustin, 1996).

Total Porosity

Total porosity is determined by mercury immersion (bulk density) coupled with helium pycnometry (skeletal density). Samples (30 g) are crushed between 20 and 30 mesh sizes (841 and 595 μm) and dried at 110°C to determine the skeletal density by helium pycnometry at pressure less than 25 psia. The total porosity is calculated from the difference between the bulk and skeletal densities.

Focused Ion Beam Milling and Field Emission Scanning Electron Microscopy

Scanning electron microscopy was performed on the Barnett and Haynesville samples at the Nanofabrication Laboratory at the University of Western Ontario, Canada and the Doig, Woodford, and Marcellus samples at the Advanced Microscopy Facility at the University of Victoria, Canada. The Barnett and Haynesville samples were placed onto aluminum mounts using carbon adhesive tabs. The FIB system focuses a beam of gallium ions to mill a region of interest with nanometer-scale precision, whereas imaging was performed using an accelerating voltage of 1.0 kV. A LEO (Zeiss) 1540 XB FE-SEM, equipped with an FIB system, was used to section the samples and examine shale porosity. An Oxford Instruments' INCA x-sight EDS, with an operating voltage of 10 kV, was used for elemental analysis. The Doig, Woodford, and Marcellus samples were carbon cemented on carbon mounts and milled on a Hitachi FB-2100 FIB system using an accelerating voltage of 2.0 kV. The FE-SEM was performed on a Hitachi S-4800 FE-SEM microscope with an accelerating voltage of 1.0 kV. The EDS was measured using a Bruker

Table 1. Reservoir Characteristics of the Sample Suite*

Shale Sample	Depth (m)	Total Porosity (%)	Mesopore/Macropore Volume (mL/100 g)	Micropore Volume (mL/100 g)	Median Pore Diameter (nm)	TOC Content (%)	% R_o
Haynesville	4000	6.2	2.6	0.1	4.9	4.2	2.37
Doig siltstone	2728	6.6	2.6	0.2	55	0.7	1.45
Woodford	3721	4.7	1.9	0.6	5.5	2.0	1.51
Marcellus	2583	3.7	1.4	0.8	3.9	3.8	1.56
Barnett	1957	3.0	1.3	0.4	4.0	3.2	2.25
Doig phosphate	2793	2.5	1.0	0.7	15.5	6.8	1.45

*Include the total porosity, the sum of the mesopore and macropore volumes, the micropore volumes, the median pore diameter, the total organic carbon (TOC) content, and the maturity (% R_o).

Quantax EDS spectrometer with accelerating voltage of 13 kV.

The FIB system at the University of Western Ontario was also used to create a thin section of the Barnett Shale for examination using TEM. The surrounding substrate was removed using the FIB to create a 1- μm thick section that was subsequently lifted from the sample using a nanomanipulator and thinned using the FIB to an approximate thickness of 100 nm. Imaging was conducted at the Biotron Imaging and Data Analysis Facility at the University of Western Ontario using a Philips CM-10 TEM set at an accelerating voltage of 100 kV, with images being captured using a Hamamatsu digital camera.

Limitations of FE-SEM and TEM nanometer-scaled pore image analyses include (1) trench size and upscaling, (2) the grain size of samples, and (3) the unconfined (no effective stress) state of pore structures. Because of cost and time constraints, only one or two trenches measuring $30 \times 40 \mu\text{m}$ were cut for each sample. Limiting the observations to these dimensions cannot be representative of the sample or upscaled to a shale reservoir because of (1) the large reservoir volumes of gas shale plays (i.e., one frac stage $\sim 3 \times 10^{-6} \text{ m}^3$ or $1 \times 10^{-8} \text{ ft}^3$) and (2) the small-scaled (millimeter to centimeter) stratigraphic and lateral heterogeneity of shale strata. To visually quantify the PSD, the FIB and FE-SEM technique would require a large number of trenches per sample (500,000 trenches cover a $2 \times 3 \text{ cm}$ thin section) from a representative suite of samples to become statistically valid. At the current trench dimensions, samples that are coarser

grained than mudrock or shale will have less mineral grains and associated pores exposed compared with finer grained samples. For instance, a siltstone has greater than two thirds of its grain size ranging between 2 and $62.5 \mu\text{m}$ (Folk, 1980), with the trench sizes at approximately $40 \times 30 \mu\text{m}$; a siltstone can be dominated by only one or several mineral grains. The size of the kerogen particles can also cause sampling problems. Dispersed organic matter in gas shales can be large particles of amorphous kerogen or fragments of land plants, and depending on the location of the trench, the kerogen can take up a large proportion of the milled surface. Samples are at a very low pressure (i.e., 3×10^{-9} psia) during image analysis, and because organic-rich shales have a high compression ratio, it is assumed that the observed pore geometries, particularly in organic matter, are different from the pore geometries at in-situ pressures within the reservoir. The creation of microfractures may also occur once a sample is removed from the in-situ conditions during core retrieval.

Organic Geochemistry and Petrology

Organic geochemistry was determined by a Rock-Eval II apparatus with total organic carbon (TOC) module. The TOC is calculated from the amount of CO_2 evolved during hydrocarbon generation and also during oxidation at 650°C . Maturity of the samples was determined from T_{max} values in degrees Celsius, which is the temperature at the S2 peak maximum. The S2 peaks were too small or nonexistent to determine maturity for all but

Table 2. Mineralogical Composition of the Sample Suite*

Sample ID	Quartz	Illite	Kaolinite	Chlorite	Total			Gypsum	Pyrite	Apatite	Calcite	Siderite	Dolomite	Total
					Clay	Feldspar	Carbonate							
Haynesville	24.1	43.2	0.9	0.6	44.7	6.6	0.0	2.5	0.0	17.9	0.0	3.0	20.9	
Doig siltstone	58.5	5.5	0.0	0.0	5.5	15.2	0.0	0.6	1.2	1.8	0.0	17.3	19.1	
Woodford	32.0	41.0	1.4	3.4	45.8	9.0	0.0	3.1	0.0	6.2	0.0	3.9	10.1	
Marcellus	28.7	33.6	3.4	6.0	43.0	21.3	0.0	0.6	0.0	3.5	3.0	0.0	6.5	
Barnett	46.7	31.4	3.8	1.1	36.3	3.8	1.0	3.0	1.5	5.7	0.9	1.2	7.8	
Doig phosphate	20.4	10.5	0.0	0.0	10.5	18.3	0.0	2.1	3.9	22.4	0.0	22.6	45.0	

*From x-ray diffraction and Reitveld Refinement (Rietveld, 1967).

one sample, and mean random vitrinite reflectance (R_o) on the dispersed organic matter (50 points) was performed in accordance with the ASTM D2798-99 standard.

Mineralogy

Crushed samples (<250 μm) were mixed with ethanol, hand ground in a mortar and pestle, and then smear mounted on glass slides for x-ray diffraction analysis. A normal-focus Cobalt x-ray tube was used on a Siemens[®] Diffraktometer D5000 at 40 kV and 40 mA. A semiquantitative estimation of the mineral content of samples was determined

using Reitveld analysis (Rietveld, 1967), which fits a polynomial curve to the diffractograms.

RESULTS

Results from the total porosity, organic geochemistry, porosimetry, vitrinite reflectance, and surface area analysis are shown in Table 1 with the mineralogy of all samples shown in Table 2 and summarized in a ternary diagram (Figure 2).

The Barnett, Marcellus, and Woodford samples are clay and quartz rich, with the Marcellus also enriched in feldspar (Table 2; Figure 2). The

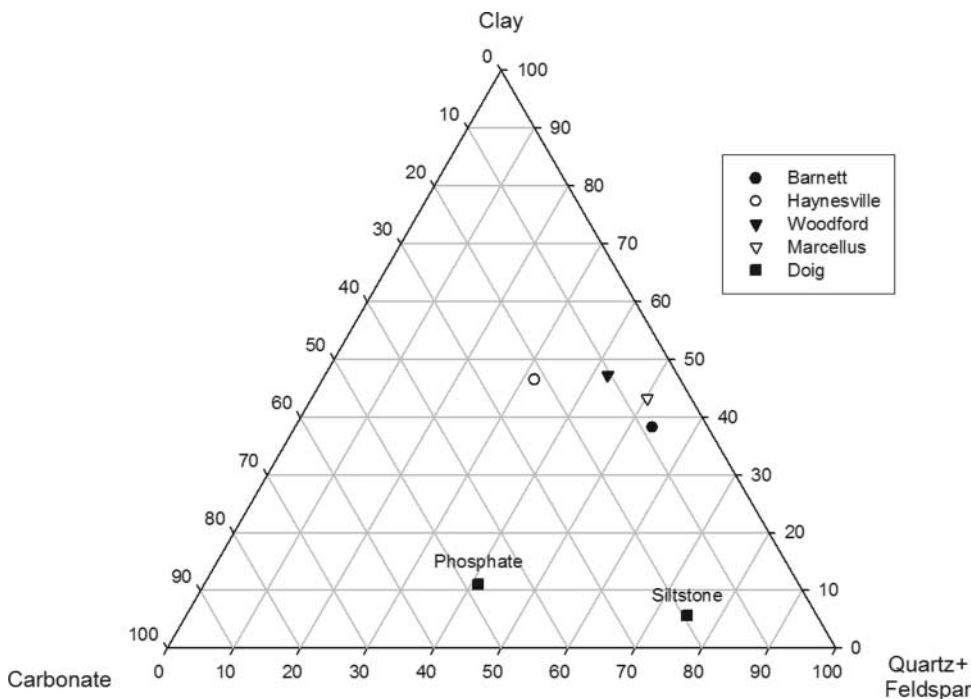
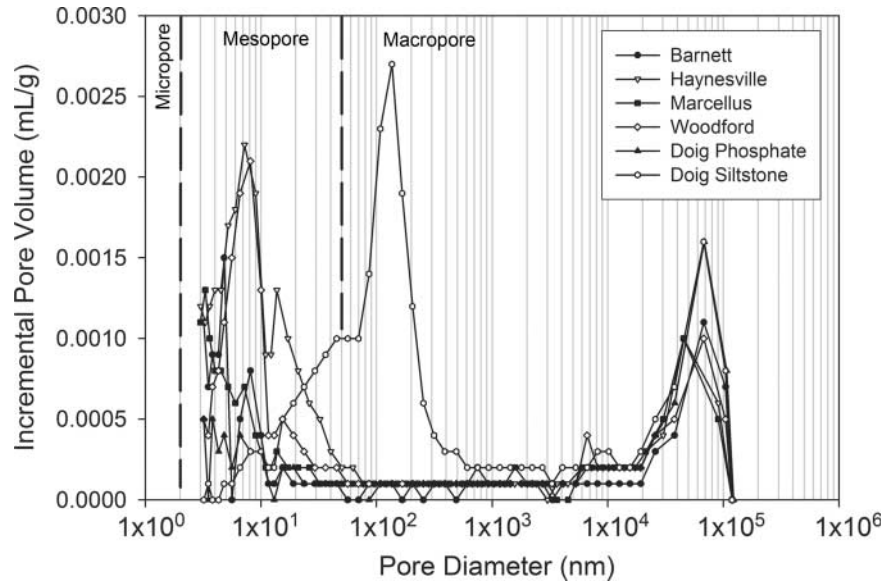


Figure 2. The mineralogical ternary diagram summarizes the composition based on the normalized data from Table 2.

Figure 3. Pore-size distribution defined by the pore volume from porosimetry analyses. Pore diameter ranges between 3 nm and 100 μm . The boundaries between micropores, mesopores, and macropores are highlighted by bold dashed lines.

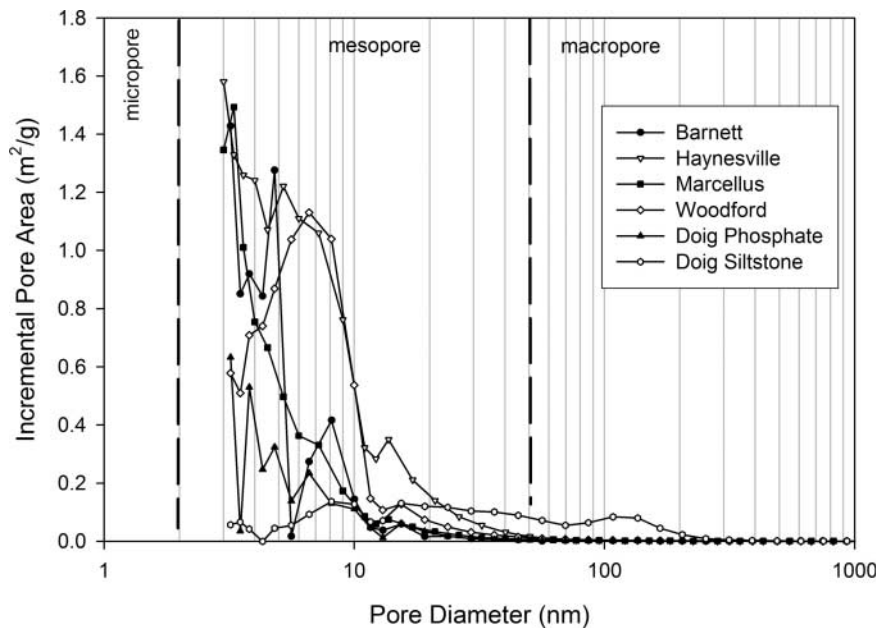


Haynesville sample is also clay and quartz rich but contains a greater amount of calcite than the other gas shale samples in the United States. The Doig samples are both clay poor and quartz and feldspar rich; however, the Doig phosphate is dominated by the carbonate minerals, calcite and dolomite. Mean random R_o ranges between 1.45 and 2.37% (Table 1). The Doig, Woodford, and Marcellus samples have similar values approximately 1.45 to 1.51%. The Barnett and Haynesville have similar maturity, with mean random R_o of

2.25 and 2.37%, respectively. All these shales are within the dry gas generation window.

The total porosity ranges between 2.5 and 6.6% (Table 1). Parameters derived from the PSD analyses include the sum of the mesopore and macropore volume, the micropore volume, and the median pore diameter (Table 1). Samples with the highest total porosities contain the greatest volume of the sum of mesopore and macropore volumes (i.e., Haynesville and Doig siltstone; Table 1). Total porosity decreases with decreasing mesopore

Figure 4. Pore-size distribution defined by the pore (surface) area from porosimetry analyses. Pore diameter ranges between 3 nm and 100 μm . The minimum pore diameter is caused by the limitations of the instrument. The boundaries between micropores, mesopores, and macropores are highlighted by dashed lines.



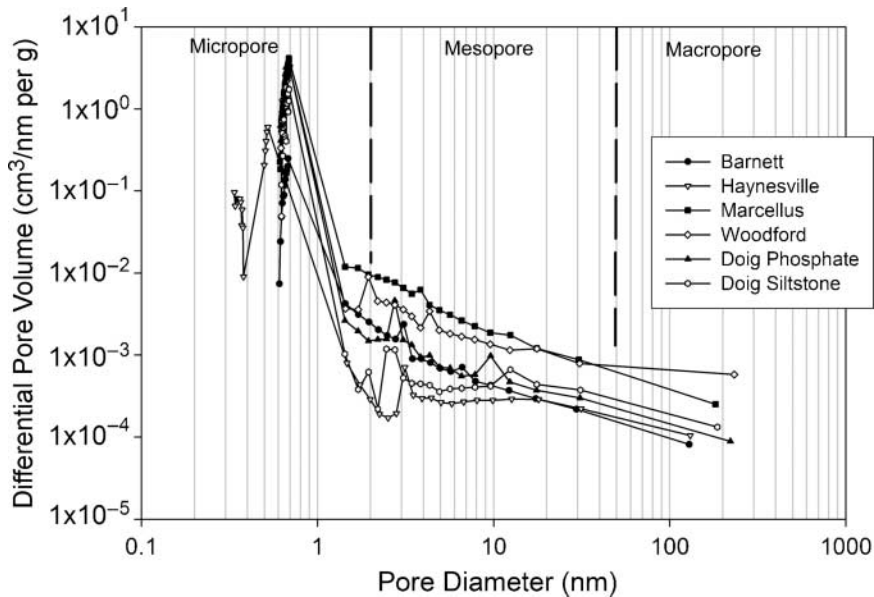


Figure 5. Pore-size distribution defined by differential pore volume using low-pressure gas (N_2 and CO_2) adsorption analyses. Pore diameters range between 0.3 and 300 nm.

and/or macropore volume and with an increase in micropore volume, with the exception of the Barnett sample. No correlation exists between the TOC content and the micropore volume (Table 1). The PSD by mercury porosimetry is plotted as incremental pore volume (mL/g ; Figure 3) and incremental pore (surface) area (m^2/g ; Figure 4). All samples show a significant volume of pores with a diameter between 10 and 100 μm (Figure 3); however, these pores do not contribute to the surface area of the reservoir as significantly as the finer pores (i.e., Doig siltstone; Figure 4). Samples with

higher surface area contain higher micropore volumes (i.e., Haynesville Formation) than samples that have low surface area measurements (i.e., Doig siltstone). Artificial intergranular porosity caused by partial filling of the penetrometer during the preparation stage of analysis may contribute to the pore volumes between 10 and 100 μm .

The Barnett, Haynesville, Marcellus, Woodford, and the Doig phosphate samples show a significant part of the pore volume between the diameters of 3 and 50 nm (mesopore size fraction) that contributes to most of the surface area measured by

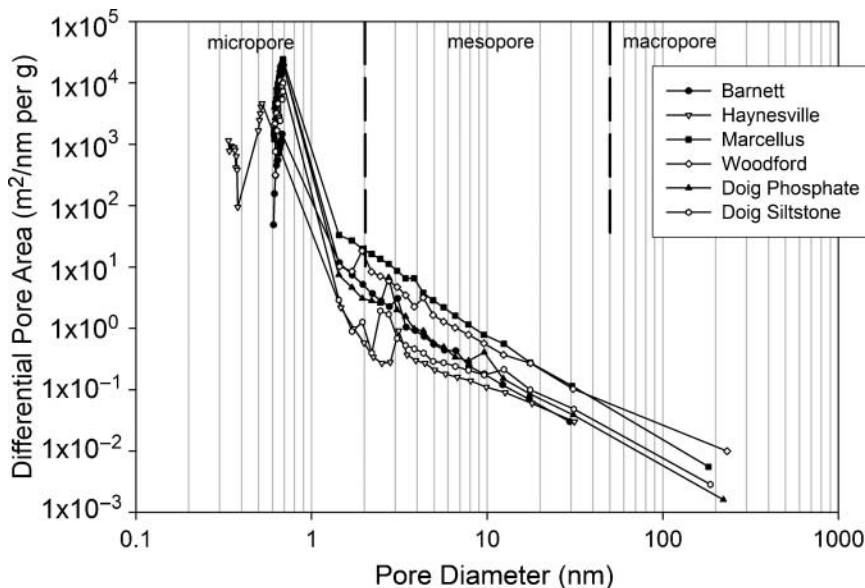
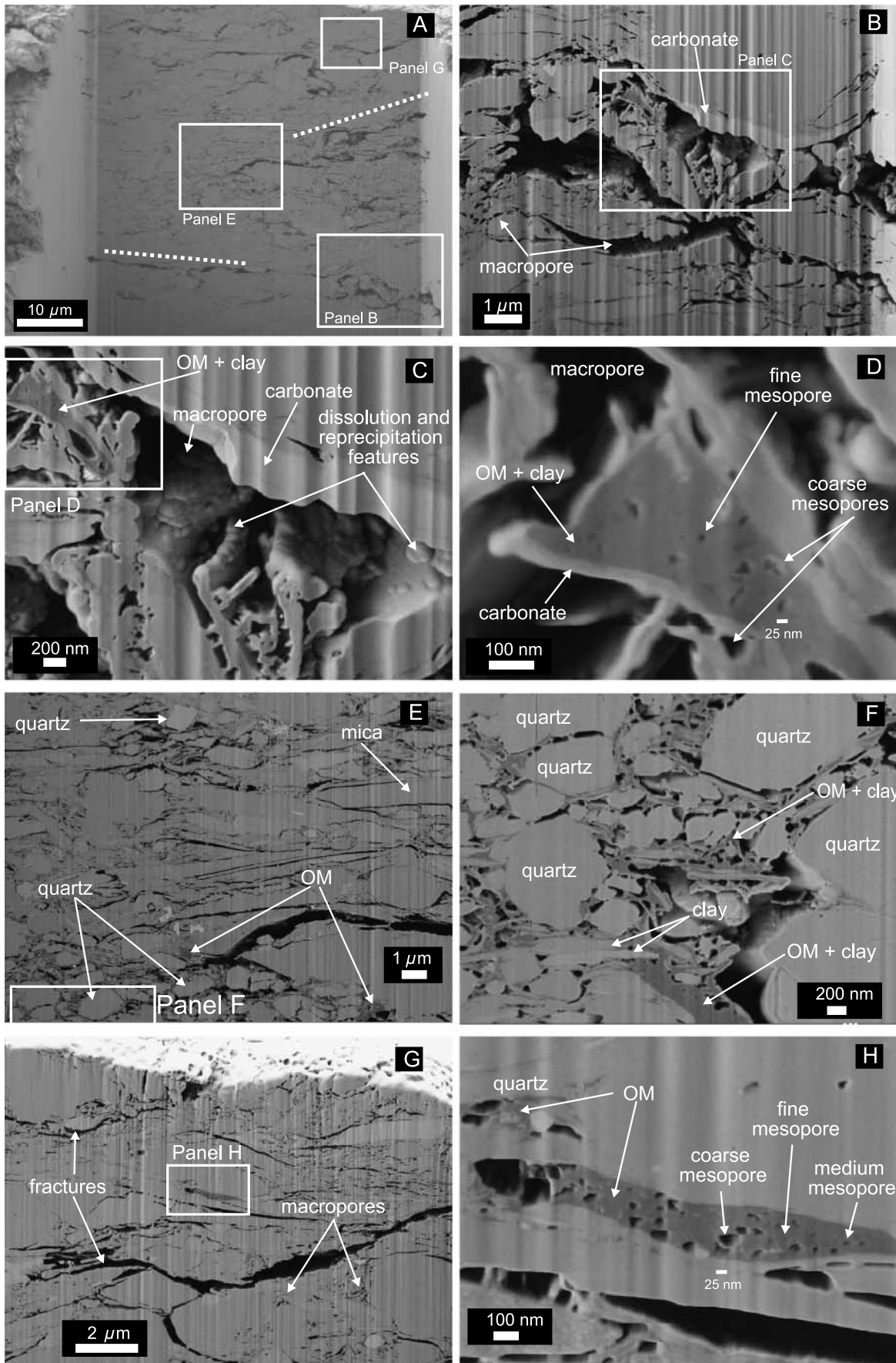


Figure 6. Pore-size distribution defined by differential pore (surface) area using low-pressure gas (N_2 and CO_2) adsorption analyses. Pore diameters range between 0.3 and 300 nm.



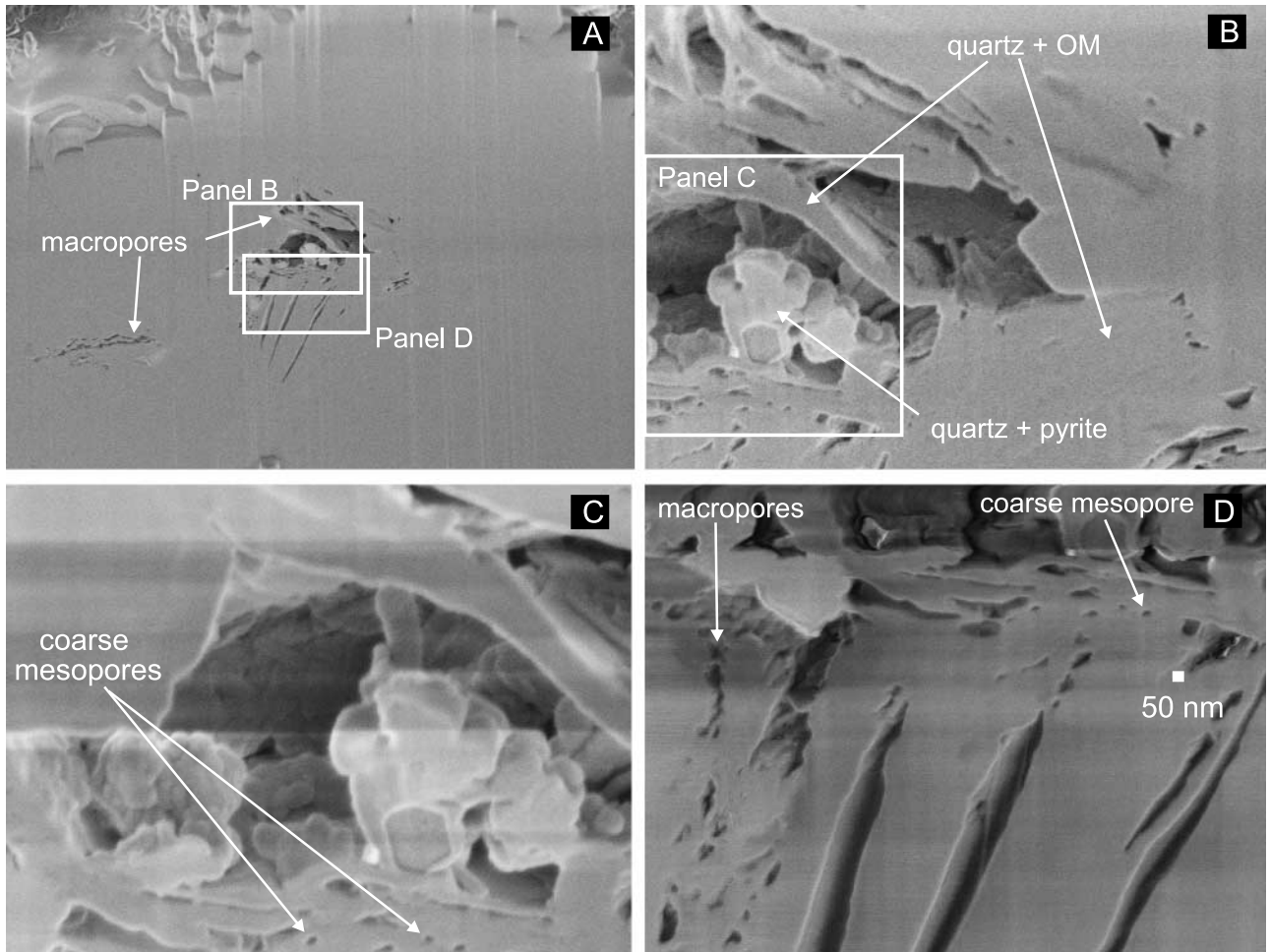


Figure 8. Field emission scanning electron microscope (FE-SEM) images of the Doig siltstone. Macropores dominated this siltstone with some coarse mesopores observed in (C) and (D). This siltstone shows limited porosity in comparison with the other samples that may reflect the larger grain size. Kerogen and quartz are identified adjacent to the pore structures from elemental analysis at 10 kV. The working distance is 6 mm, and the accelerating voltage is 1 kV. OM = organic matter.

porosimetry (Figure 3). The Doig siltstone contains a significant part of the pore volume in the macropore and coarse mesopore size ranges, particularly in the 10- to 400-nm pore diameter range. A subtle difference in the PSD exists within the mesopore size fraction between the finer grained samples, with the Haynesville and Woodford samples containing a larger part of coarse and medium mesopores (10–50 nm) and the Barnett, Doig phosphate, and Marcellus samples containing a larger part of finer mesopores (3–10 nm). The

Haynesville and Woodford samples have the highest illite contents within this study, and the illite may increase the pore volume between 10 and 50 nm.

The PSD of the mesopores and micropores is illustrated from the gas adsorption analyses using pore volume (Figure 5) and pore area (Figure 6). All samples show an increase in pore volume and surface area with decreasing pore diameter, particularly within the micropore range (<2 nm). The Marcellus sample contains the largest micropore

Figure 7. Field emission scanning electron microscope (FE-SEM) images for the Haynesville sample. The trench cut (A) with the focus on the three areas (B, E, and G). Macropores have developed because of both dissolution and reprecipitation (C), as intergranular pores (D, E, and F), induced(?) fractures (G), and with mesopores concentrating in kerogen aggregates (D and H). The working distance is 4 mm, and the accelerating voltage is 1 kV. OM = organic matter.

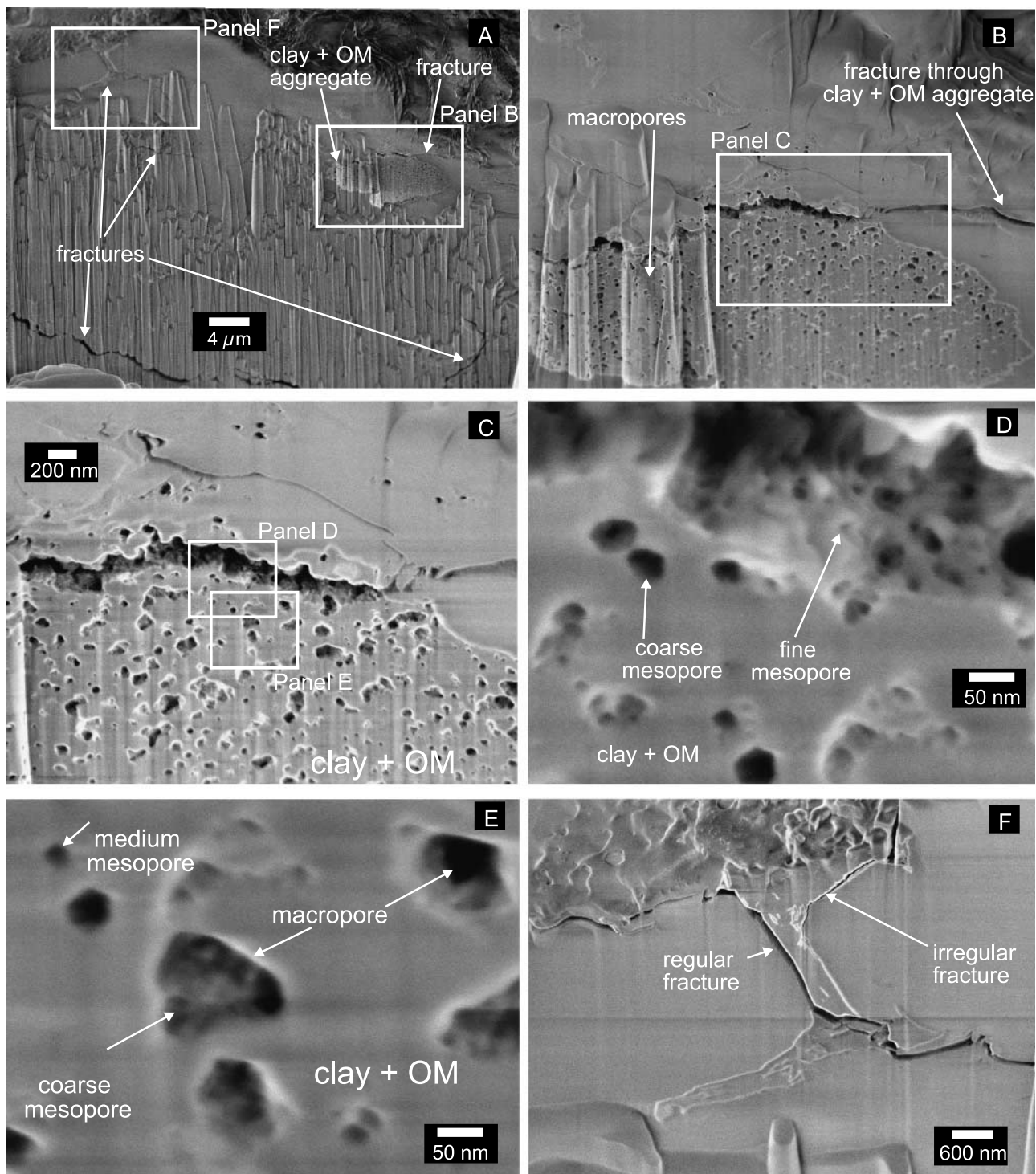


Figure 9. Field emission scanning electron microscope (FE-SEM) images of the Woodford sample. The milled surface has exposed a clay and kerogen aggregate (A and B) (elemental analysis: aluminum, silicon, carbon, oxygen, potassium). Mesopores (2–50 m [6.6–164 ft]) concentrate within the aggregate (C), and the fracture surface within the aggregate exposes fine mesopores (D; 2–10 nm). Macropores show interconnection between mesopores (E) and fracture surfaces can be either regular or irregular (F). The working distance is 5.8 mm, and the accelerating voltage is 1 kV. OM = organic matter.

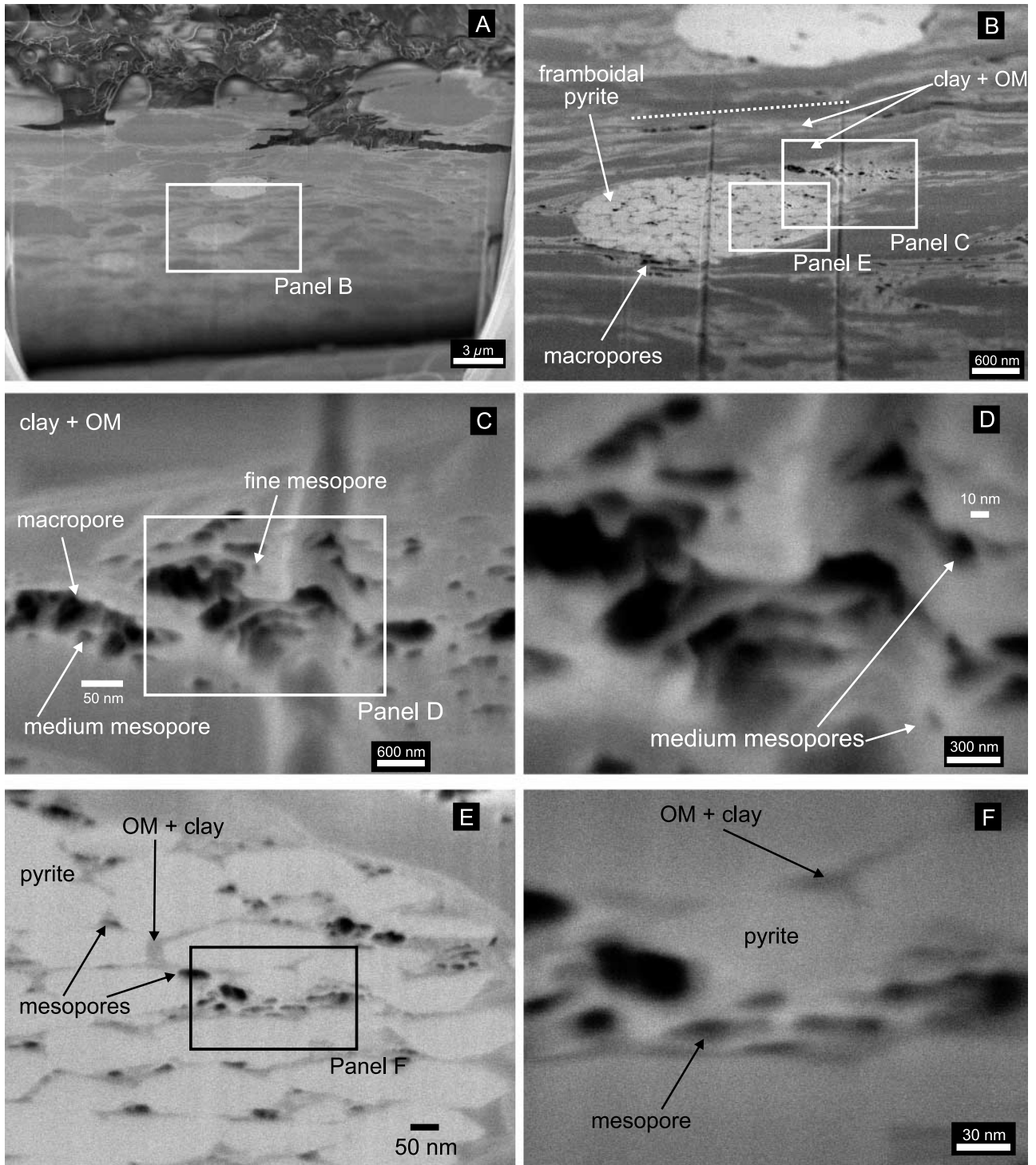
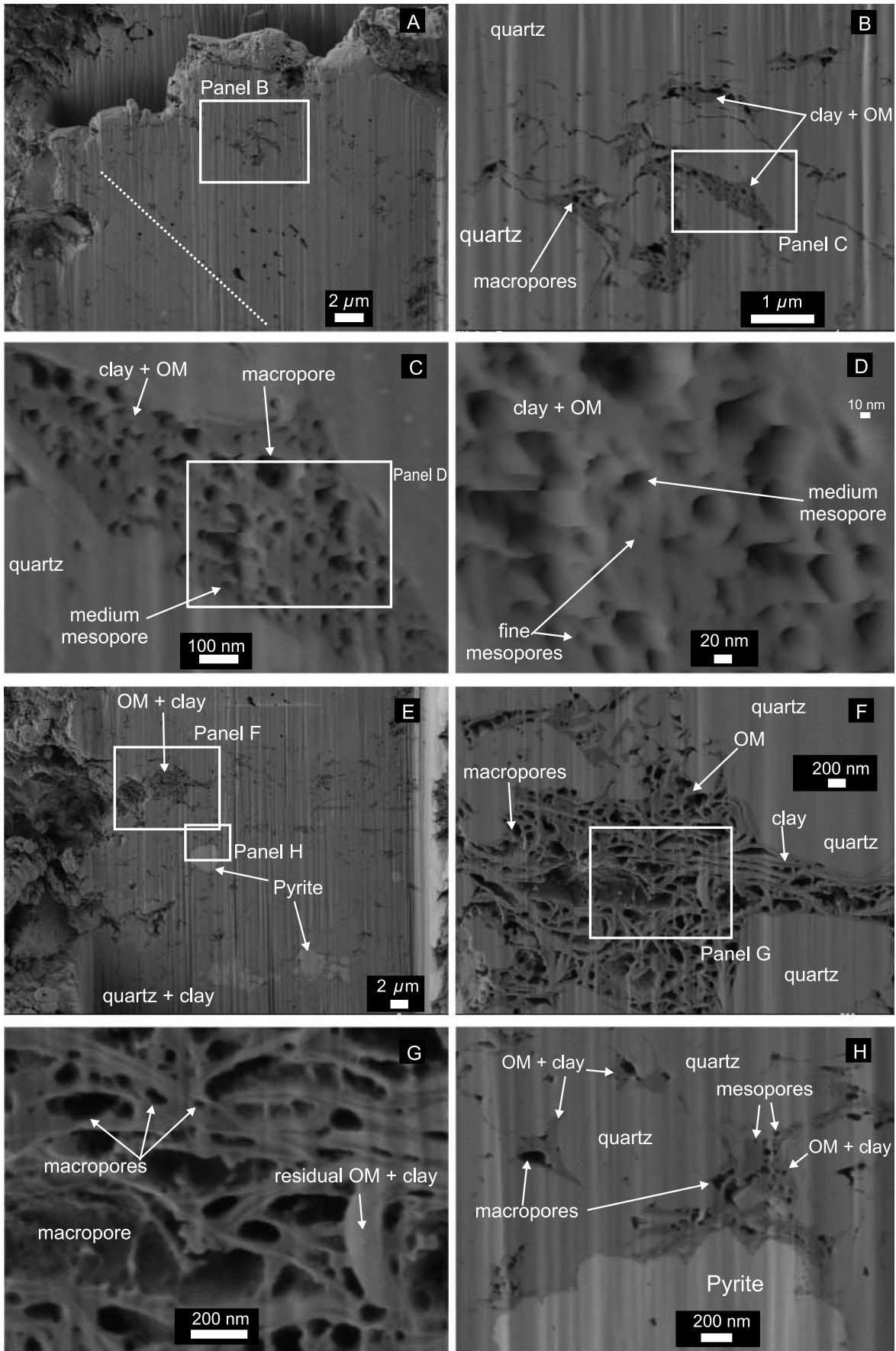


Figure 10. Field emission scanning electron microscope (FE-SEM) images of the Marcellus sample. Macropores and mesopores are located within the framboidal pyrite (B, E, and F) and are also aligned with laminations (dashed line in B). Networks of mesopores are observed with macropores (D). Note that the milled surface is not orthogonal to the detector. The working distance is 5.6 mm, and the accelerating voltage is 2 kV for (A); the working distance is 5.5 mm, and the accelerating voltage is 1 kV for (B) to (F). OM = organic matter.

and fine mesopore volumes (Figure 5) and the largest surface area between the pore diameters of 0.3 and 10 nm compared with the other samples.

The most significant contribution to surface area is from the pore diameters less than 1 nm (Figure 6). The Woodford sample contains the second largest



micropore and fine mesopore volumes and surface area, the Doig phosphate and Barnett samples showing moderate volumes and surface area, and the Haynesville and Doig siltstone contain the least. The gas adsorption analysis illustrates the importance of micropores with respect to containing the greatest amount of surface area.

The FE-SEM image and EDS analyses were performed on the Haynesville sample (Figure 7), the Doig siltstone (Figure 8), the Woodford sample (Figure 9), the Marcellus sample (Figure 10), and the Barnett sample (Figure 11). The TEM image analysis was performed on the Barnett sample (Figure 12). The FE-SEM image and EDS analyses were also performed on the Doig phosphate sample (Figure 13). The FE-SEM and TEM images (Figures 7–13) are presented in descending order of both total porosity and sum of mesopore and macropore volumes (refer to Table 2). The micropore volume increases from Figures 7–13.

The FE-SEM image and EDS analyses of the Haynesville sample illustrate a large volume of channel and vuggy macropores that may have resulted from the process of carbonate dissolution and reprecipitation (Figure 7B, C). Orientations of these macropores are either horizontal, parallel to laminae, or subhorizontal (white dashed lines in Figure 7A). Macropores are also created from dissolution of carbonate matrix or cement, creating intergranular porosity around quartz grains, clay, and kerogen (Figure 7D–F). Most of the coarse, medium, and fine mesopores (Figure 7D, H) are associated with kerogen aggregates (mixture of kerogen, clay, and carbonate). The EDS analyses show that kerogen aggregates are composed of carbon, aluminum, calcium, and silicon elements that may indicate that the kerogen contains carbonates and clay.

The quartz-rich Doig siltstone shows limited porosity with most in the macropore (Figure 8A–C) and coarse mesopore (Figure 8C, D) size fractions. Macropores have no preferred orientation

that may reflect the boundaries of large (silt-size) mineral grains. No kerogen-rich aggregates were observed within the trench, and results from EDS analysis (carbon, oxygen, and silicon) suggest that the kerogen is disseminated within a very fine quartz matrix (Figure 8B).

The Woodford samples show that most of the macropores to fine mesopores are associated within the clay and kerogen aggregates (Figure 9A–D). The sample contains one set of horizontal orientated fractures and one set of near-vertical fractures (Figure 9A, F). Horizontal fractures show an irregular surface compared with the subvertical fractures (Figure 9F). Within kerogen aggregates, fine mesopores are exposed within a horizontal fracture (Figure 9D), and coarse mesopores are observed to interconnect within macropores (Figure 9E).

Macropores and mesopores within the Marcellus sample are either aligned parallel with laminae (Figure 10B) or as intergranular pores between pyrite grains in framboids (Figure 10E, F). The intergranular space between pyrite grains contains either clay, kerogen, or pore space (Figure 10E, F). Similar to observations in the Woodford sample, macropores show interconnections with coarse to fine mesopores (Figure 10C, D).

Macropores and kerogen aggregates align parallel to laminae in the Barnett sample (Figure 11A), and a large part of macropores to fine mesopores is observed within the kerogen aggregates (Figure 11B–H). A second trench revealed kerogen and clay aggregates that contain a large volume of macroporosity, with long fibrous aggregates of clay and residual kerogen subdividing a network of macropores (Figure 11F, G). The TEM image analysis on the Barnett sample reveals that macroporosity is also associated within clay sheets (Figure 12B) and as intergranular porosity between clays and quartz grains (Figure 12C). The shale matrix contains clay, pyrite, and quartz grains as small as 15 nm (Figure 12C). Coarse to fine mesopores were identified by density changes to interconnect

Figure 11. Field emission scanning electron microscope (FE-SEM) images of the Barnett sample. Macropores and kerogen aggregates align with the laminae plane (white dotted line in A) and most of the mesopores and macropores are associated with the kerogen (B–G). From elemental analysis, kerogen is composed of aluminum, silicon, carbon, oxygen, and potassium. The working distance is 3.9 mm and the accelerating voltage is 1 kV. OM = organic matter.

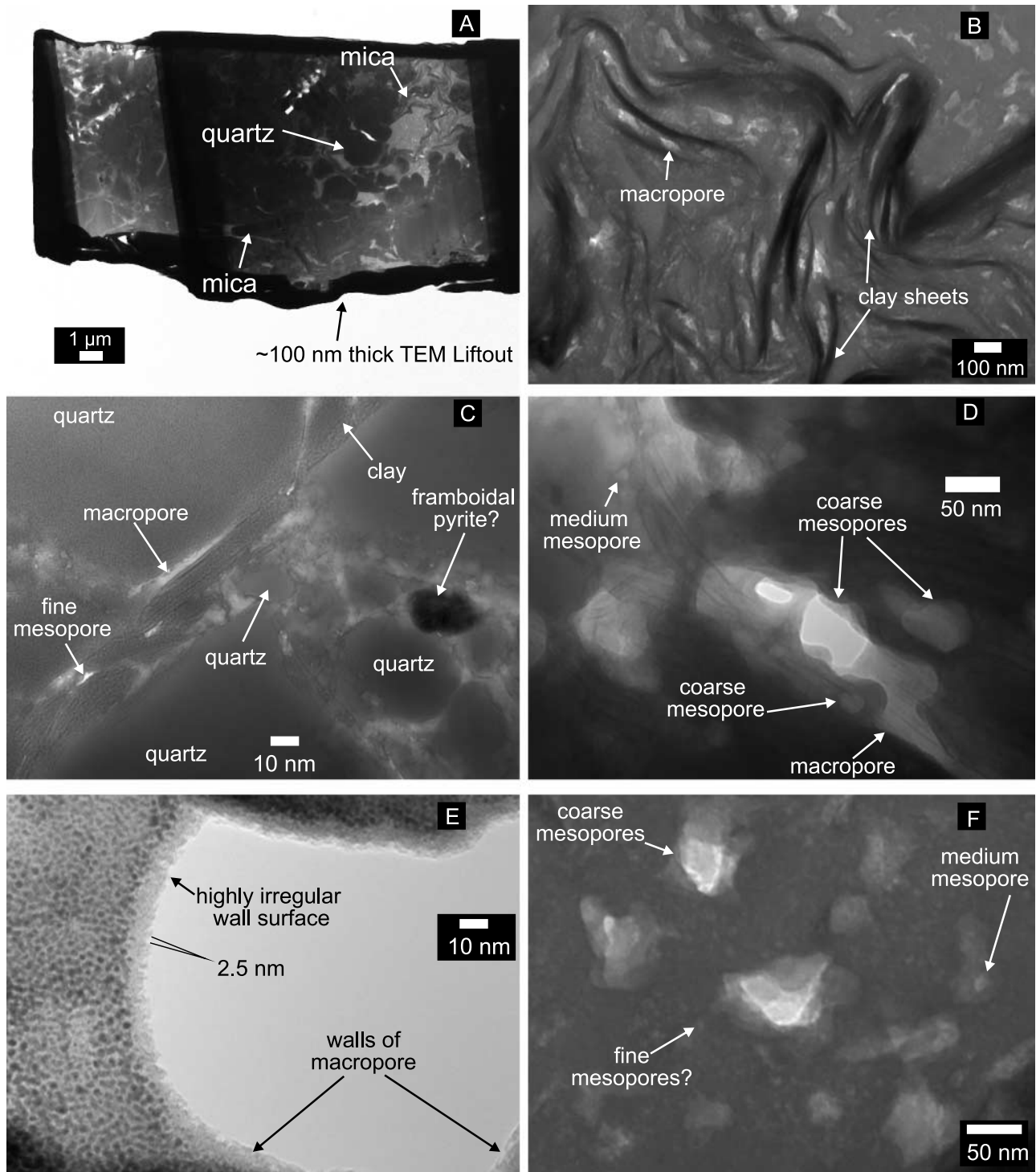


Figure 12. Transmission electron microscope (TEM) images of focused ion beam (FIB) milled 100 nm thick slab of the Barnett sample. Changes in contrast are caused by electron density changes, with darker areas being denser than lighter shaded areas. Density changes are caused by either compositional changes or thickness changes. Macropores are identified between clay layers (B) and as intergranular pores (C). Complex interconnections between mesopores are observed (D, E). The lighter shaded areas on the left side in (E) may be fine mesopores (2.5 nm) that create the irregular surface seen within the pore wall. Accelerating voltage is 100 kV.

with macropores in the TEM photomicrograph in Figure 12D. Coarse to fine mesopores are also seen in Figure 12F and also highlighted by changes in the electron density of the sample. The differences in electron density are likely a result of changes in sample thickness from the presence of fine mesopores instead of changes in sample composition. The TEM thin section also allows the observation of the irregular surface of pore walls (Figure 12E), with some of the indentations measuring approximately 2.5 nm in diameter. Micropores may cause these irregular surfaces in larger pore walls.

Macropores and mesopores are almost entirely restricted to the kerogen, clay, and carbonate aggregates within the Doig phosphate sample (Figure 13A–H). The EDS results identify carbon, aluminum, silicon, calcium, oxygen, and potassium within the aggregates. The aggregates are composed of either (1) kerogen, clay, and carbonate or (2) kerogen and carbonate. Most of the macropores and mesopores are associated with the kerogen and carbonate. A subhorizontal fracture through the kerogen, carbonate, and clay aggregate exposes the finest mesopores observed in this study (~5 nm in diameter; Figure 13E). A diagram of the diameters for the largest mesopore and micropore is superimposed in Figure 13F to highlight the difference between these two categories. Another section of the fracture surface shows interconnected mesopores and macropores, with pore throats measuring 20 nm wide (Figure 13G, H), resulting in a complex network of macropores and coarse mesopores and are also shown in Figure 13H.

DISCUSSION

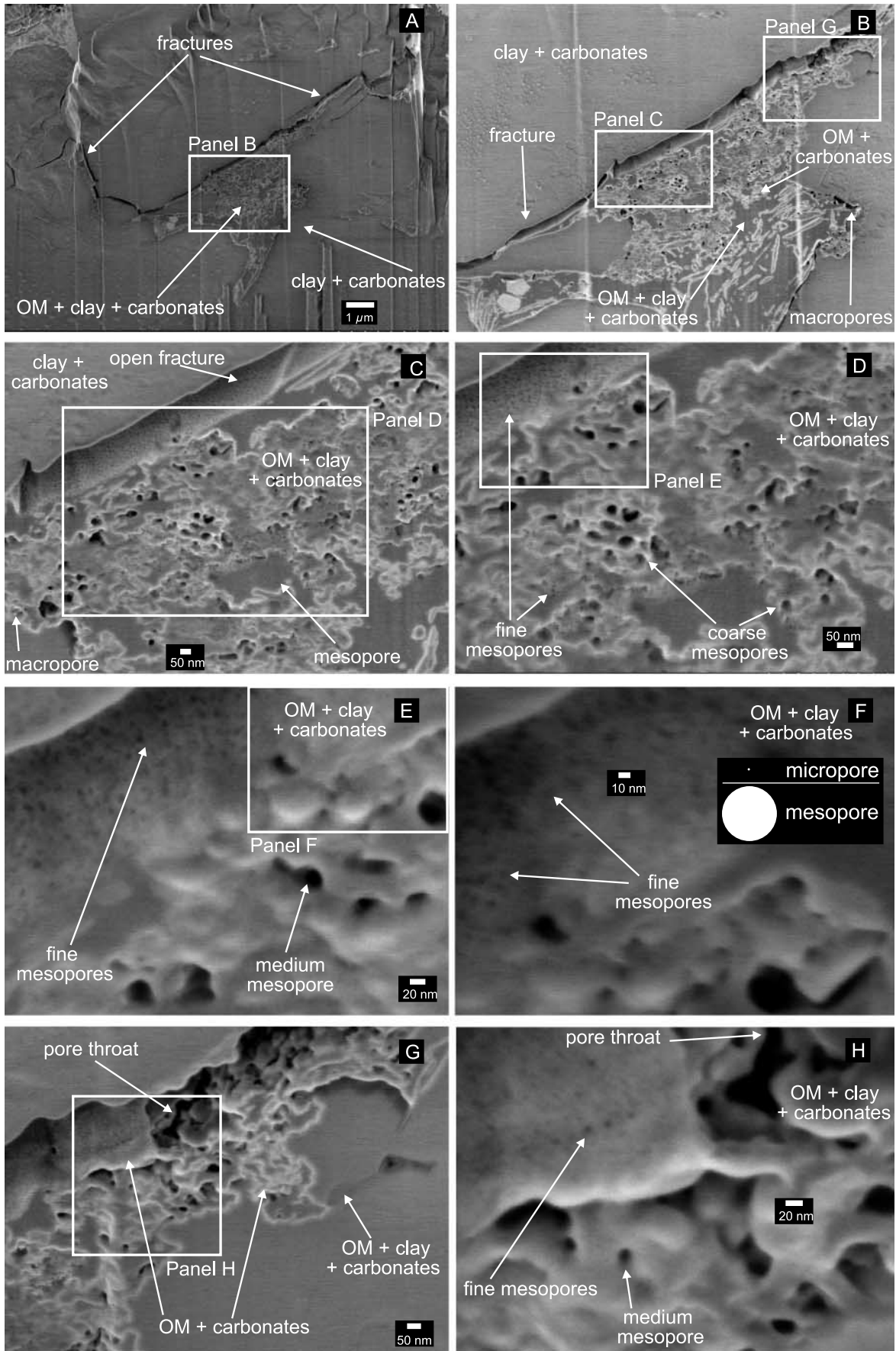
The Haynesville and Doig siltstone samples contain the largest volume of total porosity and have the largest mesopore and macropore volumes and the smallest micropore volumes (Table 1; Figures 3–6). The large volume of macropores are created by dissolution of carbonate in the Haynesville sample and illustrates the importance of paragenetic processes on the submicrometer scale. Because of the dissolution process, the macropores are well connected throughout the trench and would be im-

portant in the storage of free gas and the matrix permeability. Mesopores are observed in kerogen-rich parts of the Haynesville sample and have open communication with the intergranular macropores (Figure 7E, F).

Observations in the Doig siltstone were limited, which is caused by silt-size quartz grains reducing the number of exposed mineral grains and reducing the proportion of porosity. The Doig siltstone shows microporosity from CO₂ adsorption analyses and mesoporosity from the N₂ adsorption analysis (Figures 5, 6), and these pores are most likely to be associated with the disseminated kerogen. The EDS analysis indicates that the kerogen is finely disseminated with the quartz of the Doig siltstone (Figure 8C, D).

In general, the FE-SEM image and EDS analyses have shown that most of the macropores and mesopores are associated with either (1) kerogen and clay aggregates or (2) kerogen and carbonate aggregates. The association between mesopores and micropores with kerogen has been identified in both coalbed methane and gas shale studies (i.e., Marsh, 1987; Unsworth et al., 1989; Larsen et al., 1995; Clarkson and Bustin, 1996; Chalmers and Bustin, 2006, 2008). A large volume of macropores is also found within the kerogen of the Barnett sample (Figures 11F, G; 14). The Barnett Shale is within the dry gas window ($R_o = 2.2\%$), and the macropores are the result of the generation of hydrocarbons and associated volume loss of the kerogen. The reduction in kerogen volume is caused by organic thermal decomposition that results in the formation of hydrocarbons, residual kerogen, and increased porosity (Jarvie et al., 2007). The residual carbon-rich kerogen is observed in both photomicrographs (Figure 14A, B) and the FE-SEM images (Figure 11G, F). The reflected-light microscopic photomicrograph in Figure 14 can only distinguish large macropores.

Macropores and mesopores within the Haynesville, Barnett, and Marcellus samples concentrate along laminae. Most of the long axes of slit-shaped macropores are parallel to the laminae (Figures 7B, 10B, 11A). In the case of the Barnett sample, slit-shaped macropores are found associated with the interlayered spaces of clay particles (Figure 12B) as



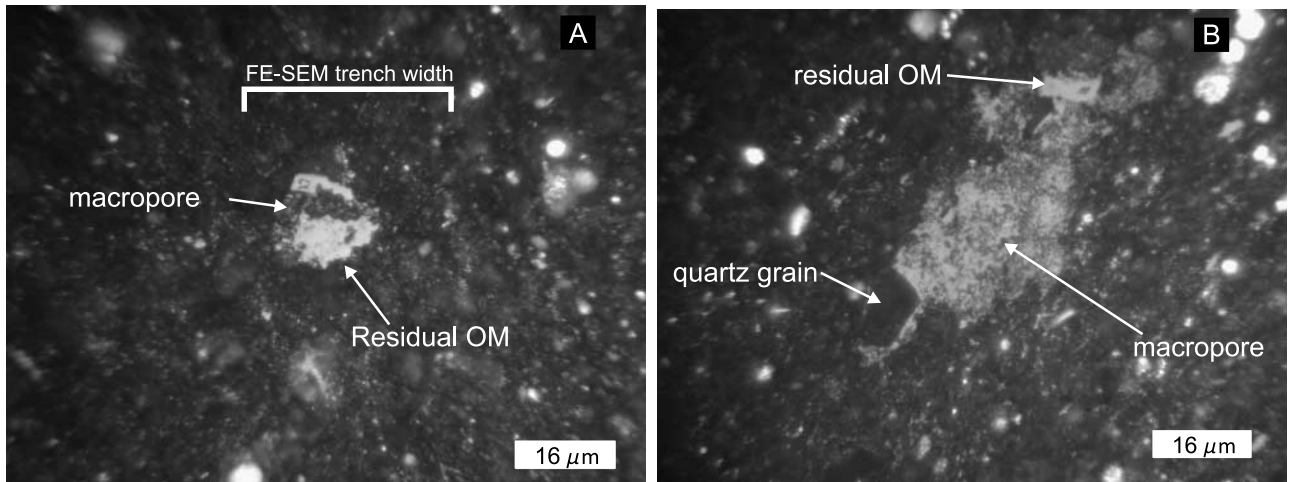


Figure 14. White-light microscopy illustrates the limitations to visual identification of pores to macropore size fraction (>50 nm). The porosity associated with the kerogen within the Barnett sample may be caused by secondary porosity produced during thermal decomposition and the formation of hydrocarbons. OM = organic matter; FE-SEM = field emission scanning electron microscopy.

well as along grain boundaries between clay and quartz grains (Figure 12C). The anisotropic fabric of shale has a large impact on permeability, with a higher permeability measured parallel to the laminae and lower permeability orthogonal to laminations (i.e., Kwon et al., 2004). The alignment of platy mineral grains (i.e., clay and mica) is a dominant control on the anisotropy and the orientation of the macropores. Fabric does not control the pore distribution in all shale samples. Macropores in the Woodford and Doig phosphate samples are confined to kerogen aggregates and show no preferred orientation. The alignment, distribution, and geometry of pores should be considered in fracture stimulation programs to maximize the intersection between macropores and induced fractures.

Networks of mesopores that connect with macropores were identified in the Woodford (Figure 9E), Marcellus (Figure 10C, D), and Doig phosphate (Figure 13G, H) samples. The TEM images of the Barnett sample provide a view of the interconnected pore structures, illustrating the complex connections between coarse to fine meso-

pores within macropores (Figure 12D). Keller et al. (2011) identified fine pores (1.5–10 nm) linking larger pores (>10 nm) in the Opalinus Clay of Switzerland. Open fractures through kerogen aggregates expose macropores and coarse, medium, and fine mesopores in kerogen aggregates (i.e., Doig phosphate sample). Interconnection between micropores, mesopores, macropores, and fractures is an important control on the matrix permeability and access to the large proportion of surface area (methane sorption sites) is located within the micropores.

Resolution of FE-SEM images on these shale samples is approximately 5 nm (Figure 13E, F). The finest mesopores (5–10 nm) were observed in the Doig phosphate and Marcellus samples. These two samples have the highest proportion of fine mesopores and micropores in the suite of shales. The highly irregular surface of the macropore wall was observed by TEM imaging of the Barnett sample, with indentations having a measured width of 2.5 nm (Figure 12E). The irregular surface could be caused by the presence of fine mesopores and

Figure 13. Field emission scanning electron microscope (FE-SEM) images of the Doig phosphate sample. This carbonate- and kerogen-rich sample shows some of the finest mesopores from the sample suite. Similar to the Woodford sample, a large part of macropores and mesopores are found within the kerogen-carbonate-clay aggregate (A–H). Along the fracture surface, the finest mesopores are exposed (C–H). Complex interconnections exist between macropores and mesopores, as illustrated in (H). The working distance is 5.7 mm, and the accelerating voltage is 1 kV. OM = organic matter.

micropores that increase the surface area of the macropore structure. No microporosity (<2 nm) was observed in the FE-SEM or TEM images. Carbon dioxide gas adsorption analysis is still the most efficient technique to assess microporosity in organic-rich sediments (Table 1).

CONCLUSIONS

Sample preparation using FIB milling coupled with high-magnification electron microscopy has provided an opportunity to image nanometer-scaled porosity in gas shale reservoirs. The FIB milling reduces surface roughness and topography to allow high-magnification imaging. Because of time and expense, this technique exposes only small areas of observation (30 × 40 μm) and cannot provide adequate sampling to characterize the sample nor the shale reservoir. The FE-SEM imaging does, however, provide a visual appreciation of pores that were once too small to observe and only proxies like gas adsorption analysis could measure and characterize. The most significant outcomes from FE-SEM and TEM image analyses follow:

1. Aggregates of kerogen, clay, and/or carbonate contain most of the macropores and mesopores in all samples.
2. Macropore development by carbonate dissolution and reprecipitation in the Haynesville sample highlights the importance of understanding the paragenesis of (carbonate-rich) shale reservoirs.
3. Macropores are either aligned parallel with laminae (anisotropic shale fabric) or show no preferred orientation as intergranular pores or within kerogen aggregates. Pore distribution and orientation will impact fracture stimulation design programs.
4. Images highlight complex pore structures in residual kerogen. A large volume of pores results from hydrocarbon generation in mature shale reservoirs.
5. The FE-SEM and TEM images provide an appreciation of the complexity of the pore networks, confirming the interconnection between

macropores with both coarse to fine mesopores. Samples with greater interconnectiveness will improve access to the surface area of the finer mesopores (and micropores) and enhance the matrix permeability of the reservoir.

REFERENCES CITED

- Barrett, E. P., L. G. Joyner, and P. P. Halenda, 1951, The determination of pore volume and area distribution in porous substances: Computations from nitrogen isotherms: *Journal of American Chemical Society*, v. 73, p. 373–380, doi:10.1021/ja01145a126.
- Beliveau, D., 1993, Honey, I shrunk the pores!: *Journal of Canadian Petroleum Technology*, v. 32, no. 8, p. 15–17.
- Boggs Jr., S., 2012, *Principles of sedimentology and stratigraphy*, 5th ed.: Upper Saddle River, New Jersey, Pearson Education, Ltd., 585 p.
- Chalmers, G. R. L., and R. M. Bustin, 2006, The organic matter distribution and methane capacity of the Lower Cretaceous strata of northeastern British Columbia, Canada: *International Journal of Coal Geology*, v. 70, no. 1–3, p. 223–23, doi:10.1016/j.coal.2006.05.001.
- Chalmers, G. R. L., and R. M. Bustin, 2007, On the effects of petrographic composition on coalbed methane sorption: *International Journal of Coal Geology*, v. 69, no. 4, p. 288–304.
- Chalmers, G. R. L., and R. M. Bustin, 2008, Lower Cretaceous gas shales in northeastern British Columbia: Part I. Geological controls on methane sorption capacity: *Bulletin of Canadian Petroleum Geology*, v. 56, no. 1, p. 1–21, doi:10.2113/gscpgbull.56.1.1.
- Clarkson, C. R., and R. M. Bustin, 1996, Variation in micropore capacity and size distribution with composition in bituminous coal of the Western Canadian sedimentary basin: Implications for coalbed methane potential: *Fuel*, v. 75, no. 13, p. 1483–1498, doi:10.1016/0016-2361(96)00142-1.
- Dollimore, D., and G. R. Heal, 1964, An improved method for the calculation of pore-size distribution from adsorption data: *Journal of Applied Chemistry*, v. 14, p. 109–114, doi:10.1002/jctb.5010140302.
- Dong, H., and D. R. Peacor, 1996, TEM observations of coherent stacking relations in smectite, I/S and illite of shales: Evidence for MacEwan crystallites and dominance of 2M1 polytypism: *Clays and Clay Minerals*, v. 44, no. 2, p. 257–275, doi:10.1346/CCMN.1996.0440211.
- Fisher, Q. J., R. A. Cliff, and M. H. Dodson, 2003, U–Pb systematics of an Upper Carboniferous black shale from South Yorkshire, United Kingdom: *Chemical Geology*, v. 194, no. 4, p. 331–347, doi:10.1016/S0009-2541(02)00383-2.
- Folk, R. L., 1980, *Petrology of sedimentary rocks*: Austin, Hemphill Publishing Company, 190 p.
- Gan, H., S. P. Nandi, and P. L. Walker, 1972, Nature of porosity in American coals: *Fuel*, v. 51, p. 272–277, doi:10.1016/0016-2361(72)90003-8.

- IUPAC (International Union of Pure and Applied Chemistry), 1994, Physical Chemistry Division Commission on Colloid and Surface Chemistry, Subcommittee on Characterization of Porous Solids: Recommendations for the characterization of porous solids (Technical Report): Pure and Applied Chemistry, v. 66, no. 8, p. 1739–1758.
- Jarvie, D. M., R. J. Hill, T. E. Ruble, and R. M. Pollastro, 2007, Unconventional shale-gas systems: The Mississippian Barnett Shale of north-central Texas as one model for thermogenic shale gas assessment: AAPG Bulletin, v. 91, no. 4, p. 475–499.
- Javadpour, F., 2009, Nanopores and apparent permeability of gas flow in mudrocks (shales and siltstones): Journal of Canadian Petroleum Technology, v. 48, no. 8, p. 16–21.
- Keller, L. M., L. Holzer, R. Wepf, and P. Gasser, 2011, 3-D geometry and topology of pore pathways in Opalinus clay: Implications for mass transport: Applied Clay Science, v. 52, p. 85–95, doi:10.1016/j.clay.2011.02.003.
- Kwon, O., A. K. Kronenberg, A. F. Gangi, B. Johnson, and B. E. Herbert, 2004, Permeability of illite-bearing shale: 1. Anisotropy and effects of clay content and loading: Journal of Geophysical Research, v. 109, no. B10205, p. 19, doi:10.1029/2004JB003052.
- Lamberson, M. N., and R. M. Bustin, 1993, Coalbed methane characteristics of Gates Formation coals, Northeastern British Columbia: Effect of maceral composition: AAPG Bulletin, v. 77, p. 2062–2072.
- Larsen, J. W., P. Hall, and P. C. Wernett, 1995, Pore structure of the Argonne premium coal: Energy and Fuels, v. 9, no. 2, p. 324–330.
- Loucks, R. G., R. M. Reed, S. Ruppel, and D. M. Jarvie, 2009, Morphology, genesis, and distribution of nanometer-scale pores in siliceous mudstones of the Mississippian Barnett Shale: Journal of Sedimentary Research, v. 79, no. 12, p. 848–861.
- Lu, G. Q., J. C. F. Low, C. Y. Liu, and A. C. Lua, 1995, Surface area development of sewage sludge during pyrolysis: Fuel, v. 74, no. 3, p. 344–348, doi:10.1016/0016-2361(95)93465-P.
- Marschall, P., S. Horseman, and T. Gimmi, 2005, Characterization of gas transport properties of the Opalinus Clay, a potential host rock formation for radioactive waste disposal: Oil and Gas Science and Technology, v. 60, p. 121–139, doi:10.2516/ogst:2005008.
- Marsh, H., 1987, Adsorption methods to study microporosity in coals and carbons: A critique: Carbon, v. 25, no. 1, p. 49–58, doi:10.1016/0008-6223(87)90039-X.
- Mastalerz, M., A. Drobniak, and J. Rupp, 2008, Meso- and micropore characteristics of coal lithotypes: Implications for CO₂ adsorption: Energy and Fuels, v. 22, p. 4049–4061, doi:10.1021/ef800544g.
- Nelson, P. H., 2009, Pore-throat sizes in sandstones, tight sandstones, and shales: AAPG Bulletin, v. 93, p. 329–340, doi:10.1306/10240808059.
- Nemeth, P., M. Tribaudino, E. Bruno, and P. Buseck, 2007, TEM investigation of Ca-rich plagioclase: Structural fluctuations related to the I1-P1 phase transition: American Mineralogist, v. 92, p. 1080–1086, doi:10.2138/am.2007.2504.
- Potter, P. E., J. B. Maynard, and P. J. Depetris, 2005, Mud and mudstones: Introduction and overview: Berlin, Germany, Springer, 304 p.
- Quantachrome, 2008, Autosorb-1/ASWin operating manual: Boynton Beach, Florida, Quantachrome Instruments, 161 p.
- Rietveld, H. M., 1967, Line profiles of neutron powder-diffraction peaks for structure refinement: Acta Crystallographica, v. 22, p. 151–152.
- Ross, D. J. K., and R. M. Bustin, 2007, Shale gas potential of the Lower Jurassic Gordondale Member, northeastern British Columbia, Canada: Bulletin of Canadian Petroleum Geology, v. 55, no. 1, p. 51–75, doi:10.2113/gscpgbull.55.1.51.
- Ross, D. J. K., and R. M. Bustin, 2008, Characterizing the shale gas resource potential of Devonian–Mississippian strata in the Western Canada sedimentary basin: Application of an integrated formation evaluation: AAPG Bulletin, v. 92, no. 1, p. 87–125, doi:10.1306/09040707048.
- Ross, D. J. K., and R. M. Bustin, 2009, The importance of shale composition and pore structure upon gas storage potential of shale gas reservoirs: Marine and Petroleum Geology, v. 26, no. 6, p. 916–927, doi:10.1016/j.marpetgeo.2008.06.004.
- Schlomer, S., and B. M. Krooss, 1997, Experimental characterization of the hydrocarbon sealing efficiency of cap rocks: Marine and Petroleum Geology, v. 14, no. 5, p. 565–580.
- Sigal, R. F., and E. Odusina, 2011, Laboratory NMR measurements on methane saturated Barnett Shale samples: Petrophysics, v. 52, p. 32–49.
- Unsworth, J. F., C. S. Fowler, and L. F. Jones, 1989, Moisture in coal: 2. Maceral effects on pore structure: Fuel, v. 68, no. 1, p. 18–26, doi:10.1016/0016-2361(89)90005-7.
- Zdravkov, B. D., J. J. Cermak, M. Sefara, and J. Janku, 2007, Pore classification in the characterization of porous materials: A perspective: Central European Journal of Chemistry, v. 5, no. 5, p. 385–395, doi:10.2478/s11532-007-0017-9.